NANOSYSTEMS:
PHYSICS, CHEMISTRY, MATHEMATICS

Aksenova E.V., et al. *Nanosystems: Phys. Chem. Math.*, 2026, **17** (1), 46–58.
http://nanojournal.ifmo.ru
DOI 10.17586/2220-8054-2026-17-1-46-58

Original article

Umbilic surfaces as a robust topological probe of 3D solitons in cholesteric liquid crystals

Elena V. Aksenova[1,a], Igor S. Lobanov[2,3,b], Tetiana Orlova[3,c], Valery M. Uzdin [1,2,d], Alexei D. Kiselev[2,e]

[1]Saint Petersburg State University, Saint Petersburg, Russia

[2]ITMO University, Saint Petersburg, Russia

[3]Institute of Physics, Yerevan State University, Yerevan, Armenia

[a]e.aksenova@spbu.ru, [b]lobanov@itmo.ru, [c]tetiana.orlova@ysu.am, [d]vmuzdin@itmo.ru, [e]adkiselev@itmo.ru

Corresponding author: E V. Aksenova, e.aksenova@spbu.ru

PACS 61.30.Jf, 64.70.Md, 42.70.Df

ABSTRACT The method based on umbilics that expose line-like organization of complex director fields is used to introduce umbilic surfaces as a numerically robust probe of three-dimensional (3D) topological solitons in frustrated cholesteric liquid crystals. We present a coordinate-free analytical formulation of the umbilic-line approach that ensures reliable detection of umbilics on discrete simulation grids and thus avoids the problems caused by instabilities and sensitivity to coordinate choices. By using our method we introduce the laboratory-referenced phase field giving a natural tool for intuitive surface colorization. In addition, we employ this field to define the two fundamental integer invariants of umbilic loops: the transverse index (the strength) and the longitudinal winding (the profile twist). These invariants directly link the umbilic geometry to the topological characteristics of textures, thus enabling soliton identification and a comparison of solitons by topological content. We apply the technique to the three canonical solitons obtained by the free-energy minimization: the toron and the looped cholesteric fingers of the first and second types with the Hopf indices equal to zero and unity, respectively. It is found that the umbilic-surface representation clearly exposes defect structures, discriminates between visually similar but topologically distinct textures and provides a tool for quantifying and visualizing 3D solitons from director field data.

KEYWORDS topological structures; umbilic lines; chiral liquid crystals; soliton; toron.

ACKNOWLEDGEMENTS The work was supported by the Ministry of Science and Higher Education of the Russian Federation, state assignments No. SER-2025-0012. I.S.L. and T.O. acknowledge the support from the Higher Education and Science Committee of RA MoESCS (Research Project No. 24IRF-1C003).

FOR CITATION Aksenova E.V., Lobanov I.S., Orlova T., Uzdin V.M., Kiselev A.D. Umbilic surfaces as a robust topological probe of 3D solitons in cholesteric liquid crystals. *Nanosystems: Phys. Chem. Math.*, 2026, **17** (1), 46–58.

1. Introduction

Topological defects in orientationally ordered systems such as liquid crystals (LCs) are universal in occurrence. The defects are of crucial importance for both understanding the fundamental properties of such systems and practical applications [1]. Typically, spatial and temporal stability of the defects in confined liquid crystals requires geometrical frustration imposed by bounding surfaces so as to inhibit the relaxation processes caused by the high cost of the elastic energy.

It is known that, in chiral nematic liquid crystals also known as the cholesteric liquid crystals (CLCs), the interplay between chirality, elasticity and surface interactions can produce topologically nontrivial localized structures (textures) [2, 3]. Specifically, in the so-called frustrated CLCs where CLC is confined between parallel plates (substrates), matching the homeotropic (perpendicular) anchoring conditions at substrates of CLC cells and the ground-state helicoidal structure cannot be done without distortion. In addition to the well-known cholesteric fingers [4], this incompatibility is known to produce a rich variety of topological soliton structures such as skyrmions, antiskyrmions, torons, bobbers, hopfions, heliknotons, and twistions [5–10]. These chirality-enabled localized structures are used as elements of singular optics [11–13] and components of diffraction gratings [14]. Note that, in magnets, chiral skyrmions [15], hopfions [16] and Bloch points in the domain walls of stressed cylindrical wires [17, 18] are well known and are often described as magnetic vortices.

Mathematically, the liquid crystal textures can be described as spatial distributions of the LC director represented by a unit vector, $\hat{\boldsymbol{n}}(\mathbf{r})$, specifying the locally averaged direction of orientation of LC molecules. The geometric characterization and corresponding accurate visualization of LC textures is a challenging task that is fundamental to understanding the

geometry and topology of LC structures. For arbitrary three-dimensional topological structures, a general theory for recognizing localized linear structures in liquid crystals, magnetic materials, or other orientationally ordered systems has yet to be developed.

In addition to characterizing geometry of LC orientational configurations in terms of preimages determined by the set of all points in the LC material where the LC molecules are aligned along a fixed direction $\hat{\boldsymbol{n}}$, a widely used visualization method for presenting complex director fields and identifying topology comes from the Pontryagin–Thom construction as applied to liquid crystals in [2]. In this method, the texture is depicted by showing the surface in space where the director field is normal to a fixed direction, say, $\hat{\boldsymbol{n}} \perp \hat{\boldsymbol{e}}_z$, where $\hat{\boldsymbol{e}}_z$ is perpendicular to the substrates of a LC cell. The surface is then colored according to the values of the azimuthal angle specifying horizontal orientation of the director on it. Note that the preimages of every orientation with a fixed z component $\hat{n}_z$ fill the surface of a torus.

Alternatively, in the umbilic-lines approach developed by Machon and Alexander [19], a general analysis of the liquid crystal director can be performed through a geometric decomposition of the gradient tensor of the director field. This method allows to identify geometrically distinguished directions and relates the defects in these directions to the topology of the texture. Selinger [20] has applied this approach to give fresh perspectives on a number of known liquid crystal structures.

In this paper, the umbilic-lines approach will be our primary concern. We propose a numerically robust and coordinate free modification of the umbilic-lines method. Based on this method, we introduce two topological indices (strength and longitudinal winding) and suggest an original coloring method for vizualizing umbilic lines. The umbilic topological indices are related to the well known topological charges such as the Hopf index [3, 21, 22] and the skyrmion number [5, 23].

For illustration purposes, we apply our method to the three numerically simulated and analytically designed soliton structures: (a) the toron; (b) the cholesteric finger (CF) loop of the first type (CF1-loop); and (c) the cholesteric finger loop of the second type (CF2-loop). The toron is a metastable topological structure with a double-twist toroidal core and two hyperbolic point defects above and below the torus plane [5,24,25]. The loop of the first type cholesteric finger possesses two pairs of nonsingular disclination circles [25–27]. The CF2-loop carries Hopf index $Q_H = 1$ (see [3]); we therefore use the term "hopfion" interchangeably with "CF2-loop". The hopfion is a topological soliton with a knotted topological structure. Isolines of the hopfion director field are closed loops which are linked together [3, 21, 22]. We show how the umbilic-lines approach clarifies the defect structure and topological content of these textures.

The paper is organized as follows. In Sec. 2 we briefly discuss numerical modeling employed for simulation of the director field distributions using the lattice model derived as a discretization of the LC free energy functional. The umbilic-lines approach and its numerical implementation are described in Sec. 3. In Sec. 4, we introduce two independent integer invariants of umbilic loops and propose the method of umbilic-lines visualization. In Sec. 5 we describe the analytical modeling procedure that uses suitably designed director field ansatzes starting from the CF1-loop configuration. The results for the topological solitons are presented in Sec. 6. Finally, we draw the results together in Sec. 7 and make concluding remarks in Sec. 8.

2. Model

The topological solitons in CLCs are 3D orientational structures determined by the CLC director field $\hat{\boldsymbol{n}}(\mathbf{r})$. From here on, a hat indicates unit vectors. Although the physical director is a line field $\hat{\boldsymbol{n}} \sim -\hat{\boldsymbol{n}}$, throughout this work we restrict to textures (and to the specific domains/surfaces used in our constructions) where $\hat{\boldsymbol{n}}$ can be chosen continuously, i.e. a global sign convention exists. All subsequent notions that use an oriented director field (in particular, the integer windings) are understood in this sense. In the presence of sign frustration (when such a continuous choice is impossible), the phase-based constructions would require a separate treatment, which is outside the scope of the present work.

In this section, we introduce numerical procedure for finding director field $\hat{\boldsymbol{n}}(\mathbf{r})$ of the topological solitons (such as torons, CF1-loop and CF2-loop (hopfion)) in the frustrated CLC.

We consider a CLC with the volume V confined in the slab geometry where the CLC is sandwiched between two parallel bounding plates (substrates): $z = -L/2$ and $z = L/2$. In this geometry, L is the thickness of the CLC cell and the z axis is normal to the substrates. Both lateral sizes of the CLC cell are equal to L_W, $L_W \gg L$, $V = LL_W^2$.

For the frustrated CLC we consider homeotropic orientation on the bounding plates: $\hat{\boldsymbol{n}}|_{z=\pm L/2} = \hat{\boldsymbol{e}}_z \equiv (0, 0, 1)$. The anchoring conditions are considered to be strong for both the bounding plates and the lateral surfaces of the sample. This confinement frustrates the intrinsic cholesteric twist and allows metastable localized structures to appear as local minima of the elastic free energy.

We model the director configurations of a cholesteric liquid crystal by minimizing the Frank–Oseen free-energy functional in a three-dimensional domain V. The free energy is (see, e.g., [28])

$$F[\hat{\boldsymbol{n}}] = \int\limits_V \left[\frac{K_1}{2}(\nabla \cdot \hat{\boldsymbol{n}})^2 + \frac{K_2}{2}(\hat{\boldsymbol{n}} \cdot \nabla \times \hat{\boldsymbol{n}} + q_0)^2 + \frac{K_3}{2}(\hat{\boldsymbol{n}} \times \nabla \times \hat{\boldsymbol{n}})^2 \right] d\mathbf{r}, \tag{1}$$

K_1, K_2, K_3 are the splay, twist and bend Frank elastic constants, respectively; $q_0 = 2\pi/P_0$ is the twisting wave number; and P_0 is the equilibrium CLC pitch. In order to find the director distributions representing metastable CLC structures, the elastic free energy (1) has to be minimized.

Assuming the simplified model of CLC director dynamics where the coupling between the director and the fluid flow can be neglected, relaxation of the director field is governed by the following dynamic equation:

$$\frac{d\hat{\boldsymbol{n}}}{dt} = -\eta \frac{\delta F[\hat{\boldsymbol{n}}]}{\delta \hat{\boldsymbol{n}}}, \tag{2}$$

where η is the rotational viscosity and the functional derivative $\dfrac{\delta F}{\delta \hat{\boldsymbol{n}}}$ is of the following form [10]

$$\frac{\delta F[\hat{\boldsymbol{n}}]}{\delta \hat{\boldsymbol{n}}} = -K_1 \nabla(\nabla \cdot \hat{\boldsymbol{n}}) - K_3[\Delta \hat{\boldsymbol{n}} - \nabla(\nabla \cdot \hat{\boldsymbol{n}})] + (K_2 - K_3)[2(\hat{\boldsymbol{n}} \cdot \nabla \times \hat{\boldsymbol{n}})(\nabla \times \hat{\boldsymbol{n}}) - \hat{\boldsymbol{n}} \times \nabla(\hat{\boldsymbol{n}} \cdot \nabla \times \hat{\boldsymbol{n}})] + 2K_2 q_0 \nabla \times \hat{\boldsymbol{n}}. \tag{3}$$

Steady states of Eq. (2) correspond to stationary points of the functional (1); in particular, metastable solitons correspond to local minima.

Here, we limit ourselves to considering the free energy and the relaxation equations for the director field. A more accurate but computationally expensive method is based on considering the tensor order parameter rather than the director field [28, 29].

To solve the problem numerically, we discretize the free energy (1) on a simple cubic lattice inside the rectangular cell and apply the finite difference method to Eq. (2). In this lattice model, directors are localized at the points of a simple cubic lattice inside the rectangular cell and we fix the unit length of the directors. The numerical procedures are implemented in the software package LCSim [30] that was extensively used in our simulations. As an initial approximation for the director field, we use the analytical ansatzes constructed in Sec. 5, which are designed to lie in the attraction basins of the target metastable solitons. In our simulations we choose the Frank constants and rotational viscosity corresponding to the nematic liquid crystal E7. In order to get the topological structures of interests as steady states, the equilibrium CLC pitch should be of the order of the thickness of the LC sample, $P_0 \sim L$.

3. Numerical extraction of umbilic lines

The umbilic-lines approach is proposed by Machon and Alexander for analysis and visualization of three-dimensional structures [19]. The starting point of this approach is the geometric decomposition of the gradient tensor of the director field $\hat{\boldsymbol{n}}$ given by (see, e.g., [20] for a simple derivation of the decomposition formula)

$$\nabla_i \hat{n}_j = \hat{n}_i (\hat{\boldsymbol{n}} \cdot \nabla)\hat{n}_j + \frac{1}{2}(\nabla \cdot \hat{\boldsymbol{n}})(\delta_{ij} - \hat{n}_i \hat{n}_j) + \frac{1}{2}(\hat{\boldsymbol{n}} \cdot \nabla \times \hat{\boldsymbol{n}})\varepsilon_{ijk}\hat{n}_k + \Delta_{ij}, \tag{4}$$

where δ_{ij} and ε_{ijk} are the Kronecker delta and the Levi-Civita symbol, respectively. The first three terms represent the derivative along the director, an isotropic transverse dilation (splay contribution), and an isotropic transverse rotation (twist contribution). The last term Δ_{ij} gives the components of the traceless symmetric tensor describing the anisotropic part of orthogonal gradients of $\hat{\boldsymbol{n}}$.

By using the well-known relation for the norm of the gradient tensor

$$\sum_{i,j} (\nabla_i \hat{n}_j)^2 = (\nabla \cdot \hat{\boldsymbol{n}})^2 + ((\hat{\boldsymbol{n}} \cdot \nabla)\hat{\boldsymbol{n}})^2 + (\hat{\boldsymbol{n}} \cdot \nabla \times \hat{\boldsymbol{n}})^2 - \nabla \cdot [\hat{\boldsymbol{n}}(\nabla \cdot \hat{\boldsymbol{n}}) - (\hat{\boldsymbol{n}} \cdot \nabla)\hat{\boldsymbol{n}}] \tag{5}$$

and orthogonality of the modes in the decomposition (4), it is not difficult to obtain the explicit expression for the norm of Δ in the form given by Machon and Alexander [19]

$$\|\Delta\|^2 \equiv \frac{1}{2}\sum_{i,j} \Delta_{ij}^2 = \frac{1}{4}(\nabla \cdot \hat{\boldsymbol{n}})^2 + \frac{1}{4}(\hat{\boldsymbol{n}} \cdot \nabla \times \hat{\boldsymbol{n}})^2 - \frac{1}{2}\nabla \cdot [\hat{\boldsymbol{n}}(\nabla \cdot \hat{\boldsymbol{n}}) - (\hat{\boldsymbol{n}} \cdot \nabla)\hat{\boldsymbol{n}}]. \tag{6}$$

The points, where Δ vanishes and $\|\Delta\|^2 = 0$, are called umbilics of the orientational order. These points correspond to the regions, where the orthogonal gradients of $\hat{\boldsymbol{n}}$ are isotropic. Except for degenerate cases, these points form one-dimensional lines. In numerical computations, however, the condition $\|\Delta\|^2 = 0$ is rarely achieved exactly due to discretization and round-off errors, so it is more robust to consider isosurfaces of small $\|\Delta\|^2$; for sufficiently small isovalues these surfaces form thin tubes enclosing the umbilic lines. Note that uniform director configuration gives $\|\Delta\|^2 = 0$, hence, solitons embedded into a uniform phase always have an umbilic at infinity.

A closely related viewpoint is obtained by restricting the gradient of $\hat{\boldsymbol{n}}$ to the transverse plane. According to [19], the decomposition formula (4) implies that the orthogonal gradient of $\hat{\boldsymbol{n}}$ can be written in the form:

$$\nabla_\perp \hat{\boldsymbol{n}} = \frac{\nabla \cdot \hat{\boldsymbol{n}}}{2} I + \frac{\hat{\boldsymbol{n}} \cdot (\nabla \times \hat{\boldsymbol{n}})}{2} J + \Delta, \tag{7}$$

where I is the identity in the plane $\hat{\boldsymbol{n}}^{\perp}$ normal to $\hat{\boldsymbol{n}}$, J is the corresponding orthogonal complex structure, and Δ is a traceless symmetric (spin–2) tensor field. In a local orthonormal frame $\{\hat{\boldsymbol{d}}_1, \hat{\boldsymbol{d}}_2\}$ of $\hat{\boldsymbol{n}}^{\perp}$ the tensor Δ can be expressed in the matrix form:

$$\Delta = \begin{pmatrix} \Delta_1 & \Delta_2 \\ \Delta_2 & -\Delta_1 \end{pmatrix}, \qquad \|\Delta\|^2 = \Delta_1^2 + \Delta_2^2, \tag{8}$$

and umbilics are precisely the zeros of Δ.

From the numerical standpoint, two practical difficulties arise if one attempts to use these continuum formulas directly. First, on a grid the director $\hat{\boldsymbol{n}}$ is known only at lattice sites; derivatives must be approximated, and higher-order derivatives are typically much noisier than lower-order ones. Second, the scalar $\|\Delta\|^2$ is nonnegative, and its vanishing generally results from cancellations between terms of comparable size; this makes direct localization of zeros from sampled data fragile, especially near the umbilic cores. Finally, the components Δ_k depend on a locally chosen transverse basis, and constructing a globally consistent family of such bases in three dimensions is challenging.

Now our task is to present a numerically robust method for detecting umbilic lines in three-dimensional CLC textures. The construction is fully tensorial, requires only first derivatives of the director field, and yields both the umbilic set and a natural phase field whose windings encode the two topological charges identified by Machon and Alexander [19]. This approach avoids the numerically ill-conditioned analytic expression (6) for $\|\Delta\|^2$, while, in the continuum limit, remaining exactly equivalent to those developed in [19].

To this end, we consider a smooth director field $\hat{\boldsymbol{n}}(\mathbf{r}) : \Omega \subset \mathbb{R}^3 \to S^2$ with $|\hat{\boldsymbol{n}}| = 1$ and assume that discrete derivatives in a cubic grid of spacing δ are implemented using centered finite differences (the notation suppresses δ since it introduces only an overall multiplicative constant in the quantities of interest). Let $\partial_l \hat{n}_i$ denote the discrete approximation to the spatial derivatives of the director and define the orthogonal projector onto the plane perpendicular to $\hat{\boldsymbol{n}}$,

$$\Pi_{ij}(\mathbf{r}) = \delta_{ij} - \hat{n}_i(\mathbf{r})\, \hat{n}_j(\mathbf{r}). \tag{9}$$

The projected gradient of the director is then given by the rank–2 tensor

$$N_{ij} = (\Pi\, \partial \hat{\boldsymbol{n}}\, \Pi)_{ij} = \Pi_{ik}\, (\partial_l \hat{n}_k)\, \Pi_{lj}. \tag{10}$$

This removes the gauge freedom of the director and discards all components of $\partial_l \hat{\boldsymbol{n}}$ parallel to $\hat{\boldsymbol{n}}$ or generated by changes of parametrization along $\hat{\boldsymbol{n}}$.

The symmetric part of N given by the relation

$$X_{ij} = \frac{1}{2}\,(N_{ij} + N_{ji}) \tag{11}$$

is a (3×3) symmetric tensor satisfying $X_{ij}\hat{n}_j = 0$. Thus X has one vanishing eigenvalue (along $\hat{\boldsymbol{n}}$) and a real two-dimensional spectrum in the orthogonal plane. These two nonzero eigenvalues encode the local curvature of the director field transverse to $\hat{\boldsymbol{n}}$ and correspond to the "principal curvatures" used in the geometric description of umbilics.

Let $\lambda_1(\mathbf{r})$ and $\lambda_2(\mathbf{r})$ stand for the eigenvalues of X restricted to the orthogonal plane and define the following two spectral invariants

$$T_1 = \mathrm{Tr}\, X = \lambda_1 + \lambda_2, \qquad T_2 = \mathrm{Tr}\,(X^2) = \lambda_1^2 + \lambda_2^2. \tag{12}$$

The traceless symmetric (spin–2) part of X, $X_0 = X - \dfrac{1}{2} T_1 \Pi$, is nonzero precisely when $\lambda_1 \neq \lambda_2$. This can be clearly seen from the scalar umbilic field defined as follows

$$\Phi(\mathbf{r}) = 2\mathrm{Tr}\,(X_0^2) = 2T_2 - T_1^2 = 2(\lambda_1^2 + \lambda_2^2) - (\lambda_1 + \lambda_2)^2 = (\lambda_1 - \lambda_2)^2. \tag{13}$$

This relation introduces the umbilic field Φ that vanishes if and only if the two principal curvatures coincide, i.e., exactly on the umbilic set. Since the director field is noisy at the grid level, we will visualize umbilics using the isosurfaces of small Φ, typically by plotting

$$\varepsilon = \log_{10} \Phi \tag{14}$$

for dynamic-range compression. Importantly, the quantity (13) is rotationally invariant and uses only first derivatives of the director field. To analyze individual umbilic lines, ε should be chosen as small as possible so that each line is enclosed by its own level surface. For sufficiently small ε the level surface is tubular; increasing the value of ε may cause isosurfaces associated with different umbilic lines to merge, create handles, and undergo other topological changes.

The traceless symmetric (spin–2) part of X, $X_0 = X - \dfrac{1}{2} T_1 \Pi$, is nonzero precisely when $\lambda_1 \neq \lambda_2$. Since, according to Eq. (6), $\|\Delta\|^2 = \dfrac{1}{2}\mathrm{Tr}\,(X_0^2)$, formula (13) implies that the umbilic field differs from $\|\Delta\|^2$ only by an irrelevant factor:

$$\Phi = (\lambda_1 - \lambda_2)^2 = 4\|\Delta\|^2. \tag{15}$$

So the zeros of Φ coincide precisely with the umbilic lines defined in the continuum theory. Therefore, our formulation provides a coordinate–free numerical realization of the Machon–Alexander spin–2 invariant.

Though the analytic expression (6) for $\|\Delta\|^2$ is elegant, it is numerically ill-conditioned for the three following reasons:

(1) It contains a divergence of a quantity already containing derivatives of $\hat{\boldsymbol{n}}$, hence requires accurate second derivatives on a discrete grid.
(2) The first two (positive) terms and the divergence term are often of similar magnitude, producing small values of $\|\Delta\|^2$ only by cancellation of large numbers. This magnifies discretization noise precisely near umbilics.
(3) The divergence is sensitive to boundary conditions, while the tensorial projection method depends only on first derivatives and is well-behaved under periodic or finite difference schemes.

For these reasons, the direct analytic evaluation of (6) is numerically unstable, whereas the projected-symmetric-tensor method provides a robust and gauge-independent alternative.

4. Index of umbilic lines and colorization of umbilic surfaces

A key advantage of the Machon–Alexander framework is that umbilics are not only a geometric diagnostic of three-dimensional textures, but also carry natural *integer-valued* topological data [19]. In their formulation, umbilics are defined as the zeros of the transverse spin–2 tensor Δ, the traceless symmetric part of $\nabla_\perp \hat{\boldsymbol{n}}$. In a local oriented orthonormal basis $\{\hat{\boldsymbol{d}}_1, \hat{\boldsymbol{d}}_2\}$ of the plane $\hat{\boldsymbol{n}}^\perp$, one may represent

$$\Delta = \begin{pmatrix} \Delta_1 & \Delta_2 \\ \Delta_2 & -\Delta_1 \end{pmatrix} = \|\Delta\| \begin{pmatrix} \cos\theta & \sin\theta \\ \sin\theta & -\cos\theta \end{pmatrix}, \qquad \Delta_1 + i\Delta_2 = \|\Delta\| e^{i\theta}, \tag{16}$$

which introduces an angle field θ (defined modulo 2π) away from the umbilic core (Machon–Alexander Eq. (9)). The umbilic index (strength) of a line U through an oriented transverse surface Σ is then the winding of θ around a small loop $C \subset \Sigma$ linking U once:

$$\mathrm{index}_\Sigma(U) = \frac{1}{2\pi} \oint_C d\theta \in \mathbb{Z} \qquad \text{(Machon–Alexander Eq. (20))}. \tag{17}$$

In our construction, the symmetric projected gradient X is supported on $\hat{\boldsymbol{n}}^\perp$, and its traceless part coincides with the Machon–Alexander spin–2 field Δ (up to an overall factor). Consequently, any phase extracted from a complex representative of the traceless part of X yields the same integer index. In particular, in any transverse basis one has

$$a + ib = 2(\Delta_1 + i\Delta_2), \qquad \arg(a + ib) = \theta, \tag{18}$$

so counting hue windings around a sufficiently small tubular level surface enclosing the umbilic core reproduces exactly the Machon–Alexander index.

The phase θ is usually introduced by expressing the spin–2 tensor Δ in an oriented orthonormal frame $\{\hat{\boldsymbol{d}}_1, \hat{\boldsymbol{d}}_2\}$ of the transverse plane $\hat{\boldsymbol{n}}^\perp$. To avoid constructing such a frame numerically, we exploit the canonical complex structure on $\hat{\boldsymbol{n}}^\perp$,

$$J\mathbf{v} := \hat{\boldsymbol{n}} \times \mathbf{v}, \qquad J^2 = -\Pi, \tag{19}$$

and build a *chiral* (spin–1) complex vector directly from a fixed real laboratory vector $\mathbf{t}$. Define

$$\mathbf{m}(\mathbf{r}) := \Pi\mathbf{t} \; - \; i\,\hat{\boldsymbol{n}} \times (\Pi\mathbf{t}) \; \in \; \hat{\boldsymbol{n}}^\perp \otimes \mathbb{C}. \tag{20}$$

A direct check gives $J\mathbf{m} = i\mathbf{m}$, i.e. $\mathbf{m}$ is a $+i$ eigenvector of J. Therefore, in any local oriented orthonormal frame $\{\hat{\boldsymbol{d}}_1, \hat{\boldsymbol{d}}_2\}$ one has

$$\mathbf{m} = \rho\, e^{i\alpha}\, (\hat{\boldsymbol{d}}_1 + i\hat{\boldsymbol{d}}_2), \qquad \rho > 0, \tag{21}$$

for some real angle field α. This simply means that the $+i$ eigenspace of J is one-dimensional over $\mathbb{C}$. We require $\Pi\mathbf{t} \neq 0$, i.e. $\mathbf{t} \nparallel \hat{\boldsymbol{n}}$ on the region of interest; in practice one may switch between two or three choices of $\mathbf{t}$.

Let $S = c\Pi$ be any isotropic transverse tensor. Then

$$\mathbf{m}^{\mathsf{T}} S\, \mathbf{m} = c\, \mathbf{m}^{\mathsf{T}} \mathbf{m}. \tag{22}$$

However, $\mathbf{m}$ is a complex null vector:

$$\mathbf{m}^{\mathsf{T}} \mathbf{m} = (\Pi\mathbf{t}) \cdot (\Pi\mathbf{t}) - (\hat{\boldsymbol{n}} \times \Pi\mathbf{t}) \cdot (\hat{\boldsymbol{n}} \times \Pi\mathbf{t}) - 2i\, (\Pi\mathbf{t}) \cdot (\hat{\boldsymbol{n}} \times \Pi\mathbf{t}) = 0, \tag{23}$$

since $|\hat{\boldsymbol{n}} \times (\Pi\mathbf{t})| = |\Pi\mathbf{t}|$ and $(\Pi\mathbf{t}) \perp (\hat{\boldsymbol{n}} \times \Pi\mathbf{t})$. Therefore, contraction with $\mathbf{m}$ automatically eliminates the isotropic part, so that only the traceless-symmetric (spin–2) component contributes.

We can now define a complex scalar field that encodes the transverse anisotropy together with a phase:

$$\zeta(\mathbf{r}) := \mathbf{m}(\mathbf{r})^{\mathsf{T}} X(\mathbf{r})\, \mathbf{m}(\mathbf{r}). \tag{24}$$

On the transverse plane one has $X = (T_1/2)\Pi + (\text{antisymmetric}) + \Delta$, and the first two terms do not contribute to (24). The isotropic term vanishes by the null property above, while the antisymmetric term vanishes by symmetry of the contraction. Consequently,

$$\zeta = \mathbf{m}^{\mathsf{T}} \Delta\, \mathbf{m} = 2\rho^2\, (\Delta_1 + i\Delta_2)\, e^{2i\alpha} = 2\rho^2 \|\Delta\| e^{i(\theta + 2\alpha)}. \tag{25}$$

Thus $\arg\zeta = \theta + 2\alpha$. On a small loop linking an umbilic line (if $\Pi\mathbf{t} \neq 0$ on the spanning disk) the angle field α is smooth and single-valued, so $\oint d\alpha = 0$ and the winding of $\arg\zeta$ equals the Machon–Alexander index.

For numerical colorization it is convenient to avoid constructing the chiral vector (20) and instead extract a phase from a fixed laboratory projection of X. We introduce two fixed traceless symmetric matrices

$$A_{ij} = \delta_{i1}\delta_{j1} - \delta_{i2}\delta_{j2}, \qquad B_{ij} = \delta_{i1}\delta_{j2} + \delta_{i2}\delta_{j1} \tag{26}$$

and define the complex scalar

$$\zeta_{\mathrm{lab}}(\mathbf{r}) := \langle A, X(\mathbf{r})\rangle + i\,\langle B, X(\mathbf{r})\rangle, \qquad \langle Y, Z\rangle := \mathrm{Tr}(Y^{\mathsf{T}} Z). \tag{27}$$

In Cartesian components, this is simply

$$a = X_{11} - X_{22}, \qquad b = X_{12} + X_{21}, \qquad \zeta_{\mathrm{lab}} = a + ib, \tag{28}$$

and we set

$$\theta_{\mathrm{lab}}(\mathbf{r}) := \arg\zeta_{\mathrm{lab}}(\mathbf{r}). \tag{29}$$

The reason is that, at each point $\mathbf{r}$, the spin–2 field $\Delta(\mathbf{r})$ lives in a two-dimensional real vector space $S(\hat{\boldsymbol{n}}(\mathbf{r}))$ (traceless symmetric bilinear forms on $\hat{\boldsymbol{n}}^{\perp}$). The laboratory map $L(M) := (\langle A, M\rangle, \langle B, M\rangle)$ restricts to a linear map $L|_{S(\hat{\boldsymbol{n}})} : S(\hat{\boldsymbol{n}}) \to \mathbb{R}^2$. A direct calculation shows that this restriction is invertible if and only if $n_z \neq 0$; more precisely,

$$\det\big(L|_{S(\hat{\boldsymbol{n}})}\big) \;\propto\; n_z\,(n_x^2 + n_y^2 + 2n_z^2), \tag{30}$$

so the only degeneracy locus on the unit sphere is the circle $n_z = 0$. Equivalently, if $n_z \neq 0$ then $a = b = 0$ implies $\Delta = 0$.

Therefore, in any region where $n_z \neq 0$, the two numbers (a, b) uniquely specify the local spin–2 tensor (up to an overall scale) and thus define the same phase as (Δ_1, Δ_2), differing only by a smooth, nonsingular linear mixing. Consequently, for any small loop C linking an umbilic line U and lying in a region where $n_z \neq 0$, the winding of θ_{lab} is equal to the Machon–Alexander umbilic index:

$$\frac{1}{2\pi}\oint_C d\theta_{\mathrm{lab}} = \frac{1}{2\pi}\oint_C d\theta = \mathrm{index}_{\Sigma}(U), \tag{31}$$

provided $\zeta \neq 0$ on the chosen tubular isosurface (so that θ_{lab} is continuous there). In practice, this condition is enforced by choosing the isosurface away from the degeneracy set $n_z = 0$ and monitoring that $|\zeta_{\mathrm{lab}}|$ does not approach zero on the rendered surface.

If $|\zeta_{\mathrm{lab}}|$ becomes (numerically) small on the rendered tubular surface, so that $\theta = \arg\zeta_{\mathrm{lab}}$ is ill-conditioned, we switch to an alternative laboratory chart obtained by a cyclic permutation of axes. Concretely, we recompute (a, b) using another coordinate pair in the plane orthogonal to $\hat{\boldsymbol{n}}$:

$$(a_x, b_x) := (X_{22} - X_{33},\, X_{23} + X_{32}) \quad (n_x \neq 0), \tag{32}$$

$$(a_y, b_y) := (X_{33} - X_{11},\, X_{31} + X_{13}) \quad (n_y \neq 0), \tag{33}$$

and set $\theta := \arg(a + ib)$ using the chart for which $|a + ib|$ stays safely away from zero on the surface. On overlaps where two charts are valid, they are related by a smooth nonsingular linear mixing of the spin–2 components, so the winding index is unchanged provided the integration contour avoids points where $a = b = 0$.

In Sec. 3 we have introduced umbilic level surfaces $\Phi = \mathrm{const}$, which form thin tubes around umbilic lines. These surfaces are more convenient for numerical analysis than the lines themselves; accordingly, they are used in a number of works, including [19, 31] and related studies. Once a phase θ is available in the laboratory frame, we can color the isosurface in a way that makes its topological content immediately visible by mapping θ to the hue of the HSL color scheme,

$$\mathrm{hue}(\mathbf{r}) = \frac{\theta(\mathbf{r})}{2\pi}. \tag{34}$$

This colorization highlights both local structure (winding around individual umbilic cores) and global organization (phase variation along closed umbilic loops) encoded by the umbilic set.

There are two independent integer-valued topological indices introduced in correspondence with ones defined by Machon and Alexander [19] and naturally associated with umbilic lines.

(i) Transverse index (strength). Let $U \subset \Omega$ be an umbilic line and choose a sufficiently small tubular neighbourhood $N_\varepsilon(U)$. Pick a point $p \in U$ and let $D_p \subset N_\varepsilon(U)$ be a small oriented *normal disk* transverse to U at p. Its positively oriented boundary $\gamma := \partial D_p$ is a *meridian* linking U once.

We will use the signed intersection number $\mathrm{Int}(U, \Sigma) \in \mathbb{Z}$ between an oriented curve U and an oriented surface Σ (assumed transverse), defined by

$$\mathrm{Int}(U, \Sigma) := \sum_{x \in U \cap \Sigma} \mathrm{sign}_x(U, \Sigma), \tag{35}$$

where $\mathrm{sign}_x(U,\Sigma) = \pm 1$ is fixed by the orientations of U and Σ as follows: $\mathrm{sign}_x(U,\Sigma) = +1$ if the positively oriented tangent to U at x, together with a positively oriented tangent basis of Σ at x, gives the positive (right-handed) orientation of the ambient domain Ω, and $\mathrm{sign}_x(U,\Sigma) = -1$ otherwise.

Assume that the chosen phase construction (in particular, the laboratory chart used to define θ) is nondegenerate on the meridian γ, so that $d\theta$ is well-defined along γ. We define the *transverse index* of U with respect to the disk D_p by

$$\mathrm{index}_{D_p} U := \frac{1}{2\pi} \oint_\gamma d\theta \in \mathbb{Z}, \tag{36}$$

and its *strength* by $s := |\mathrm{index}_{D_p} U| \in \mathbb{N}$. Equivalently, $\mathrm{index}_{D_p} U = s\,\mathrm{Int}(U, D_p)$. For generic umbilics one finds $s = 1$, whereas higher strengths may occur in axisymmetric textures.

By construction, U intersects the disk fiber D_p once and transversely. To fix orientations, we first consider an oriented tangent $\mathbf{t}$ at p. The meridian $\gamma = \partial D_p$ is then oriented by the following geometric rule: when looking along $\mathbf{t}$ (with $\mathbf{t}$ pointing towards the observer), the positively oriented traversal of γ goes counterclockwise. The orientation of the umbilic line U is then fixed by the condition $\mathrm{index}_{D_p} U > 0$.

The strength s requires only that the laboratory phase construction be nondegenerate in a small neighbourhood of the chosen meridian γ around each intersection point. If such a degeneracy is encountered, one must either switch to an alternative chart or deform the meridian within $N_\varepsilon(U)$ so that $d\theta$ remains well defined.

To connect transverse umbilic indices with the skyrmion number, we now consider an arbitrary oriented surface $\Sigma \subset \Omega$ that is transverse to all umbilic components U_i and such that $\hat{\boldsymbol{n}}$ is smooth on Σ. Machon and Alexander [19] show that the total transverse winding of umbilics through Σ reproduces the skyrmion number Q of $\hat{\boldsymbol{n}}$ on Σ, with an additional contribution associated with $\partial\Sigma$ when $\partial\Sigma \neq \varnothing$. In the simplest case when $\partial\Sigma = \varnothing$ (or, more generally, when the boundary contribution vanishes), the relation reduces to

$$\sum_i s_i\,\mathrm{Int}(U_i, \Sigma) = 4Q. \tag{37}$$

In our setting Σ is typically a planar section whose boundary lies on the boundary of the computational box. Even under homogeneous (Dirichlet) anchoring, the boundary contribution is not generically zero; rather, it can be reinterpreted after compactification. Indeed, if $\hat{\boldsymbol{n}}$ is fixed on $\partial\Omega$, one may identify all boundary points in order-parameter space and attach a "cap" closing Σ to a topological sphere. The additional intersection required for (37) is then naturally attributed to an *umbilic at infinity*: a contribution supported on (or arbitrarily close to) the boundary and induced by the homogeneous far-field/anchoring condition.

In practice we access this "umbilic at infinity" through umbilic level surfaces (isosurfaces of Δ or Φ), which typically approach the boundary over large areas. The same phase-winding measurement used for interior umbilics can then be performed on these boundary-adjacent portions, providing a direct numerical estimate for the compactification contribution.

(ii) Longitudinal profile winding. Let U be a closed umbilic loop and let N_U be a sufficiently small tubular neighbourhood of U (a solid torus) such that the phase field θ is well-defined on $N_U \setminus U$. To quantify how the transverse umbilic profile twists as one goes once around the loop, we integrate the globally defined 1-form $d\theta$ along a *preferred longitude* on the boundary torus ∂N_U.

Choose a simple closed curve $\lambda_0 \subset \partial N_U$ with linking $\mathrm{Lk}(\lambda_0, U) = 0$ that is fixed by a framing of U. For instance, one may take

$$\lambda_0 := \Sigma_U \cap \partial N_U, \tag{38}$$

where Σ_U is an oriented Seifert surface with $\partial\Sigma_U = U$. The orientation of λ_0 is chosen so that λ_0 runs along U in the same direction as the oriented tangent of U, where the orientation of U was fixed in the definition of the transverse index. We then define the *longitudinal profile winding* by

$$k \;:=\; \frac{1}{2\pi} \oint_{\lambda_0} d\theta \in \mathbb{Z}. \tag{39}$$

The integer k measures how the transverse umbilic profile twists as one goes once around the loop. The choice of λ_0 (equivalently, the framing) matters: replacing λ_0 by $\lambda_0 + m\mu$, where μ is a meridian defined above, changes k by $ms\mathrm{Int}(U, D_p)$, where s is the transverse winding. With the preferred longitude fixed as above, k is a well-defined invariant of the umbilic loop.

In particular, k is related to the self-linking of U once a canonical push-off of U is specified by the transverse profile (i.e. by a choice of framing). It also contributes to the Hopf index of the director field through the usual linking interpretation of the Hopf charge.

Thus, the same phase field θ encodes both transverse and longitudinal invariants, and the hue colorization of umbilic isosurfaces provides a direct visual readout of these windings.

5. Analytical design and soliton relaxation

To access metastable localized states in a frustrated cholesteric cell, it is advantageous to complement direct numerical relaxation with *analytical design* of initial director configurations. In this section we construct analytical director-field configurations (ansatzes) that (i) provide physically interpretable templates for common soliton textures in homeotropic CLC cells and (ii) serve as initial conditions for the energy-minimization procedure described in Sec. 2. This combination is standard in the soliton literature: a well-designed ansatz places the system in the basin of attraction of the desired local minimum, while subsequent relaxation removes any artifacts of the analytical construction and yields a numerically equilibrated texture.

Following [32,33], we begin with simple CLC structures and use these results to construct the ansatzes for cholesteric fingers of different types, as well as the CF1-loop, the toron and the CF2-loop (hopfion). The ansatz parameters used below are chosen to match the representative soliton geometries considered in our simulations and to provide reliable convergence under energy minimization.

We use the following parameters for the toron and CF1-loop ansatzes [32]. For the looped helix as a core part of the toron, the pitch and the tilt angle are $P = 15$ μm and $\tan\theta = 0.7$. The radius of the toron is $R_1 = 7$ μm. The surface-mask parameters are $d = 1.1$ μm, $p = 2$, and $\kappa = 0.7$. For CF1-loop we take $P = 12$ μm and $\tan\theta = 0.7$, with inner and outer radii $R_0 = 5$ μm and $R_1 = 23$ μm; the parameters d, p, and κ are the same as for toron.

For the energy-minimization procedure we use the following parameters [32]: the Frank constants are $K_1 = 10.5$ pN, $K_2 = 6.2$ pN, and $K_3 = 18.7$ pN, the rotational viscosity is $\eta = 203.6$ mPa·s. In the lattice model, the numbers of grid points along the normal and along each lateral direction are 40 and 240, respectively. The cell thickness is $L = 10$ μm, and both lateral sizes of the CLC cell are $L_W = 60$ μm. For the toron the helix pitch is $P_0 = 10.0$ μm, and for CF1-loop it is $P_0 = 9.0$ μm.

We model the CF2-loop following [33]. For the configuration considered here the linked-preimage construction yields Hopf index $Q_H = 1$. We use the following parameters for the hopfion ansatz. The radius R of the finger loop is 50 μm, and the ansatz parameters are $\alpha_w = 0.2$ and $A = -0.9\pi$. To find a local minimum of the energy (1) for the hopfion we use the following parameters [34, 35]: the Frank constants are $K_1 = 10.3$ pN, $K_2 = 7.4$ pN, and $K_3 = 16.5$ pN, the rotational viscosity is $\eta = 203.6$ mPa·s. The helix pitch is $P_0 = 36$ μm. In the lattice model, the numbers of grid points along the normal and along each lateral direction are 50 and 250, respectively. The cell thickness is $L = 33$ μm, and both lateral sizes of the CLC cell are $L_W = 165$ μm.

6. Visualization of topological solitons by the umbilic-lines approach

We now apply the umbilic-lines framework to representative localized structures in homeotropic cholesteric cells. We compare the relaxed configuration obtained by energy minimization and the corresponding analytical ansatz, and then interpret the umbilic set in terms of the transverse strength s and the longitudinal winding k introduced in Sec. 4. This provides a compact description of the soliton topology that complements more traditional visualizations based on director cross-sections and isolines.

Fig. 1 shows the director field (panels a and c) and the corresponding umbilic structures visualized as isosurfaces of ε (panels b and d) for the toron. Panels a and b correspond to the relaxed configuration obtained by energy minimization, whereas panels c and d show the analytical ansatz. The toron ansatz reproduces the main characteristics of the relaxed toron well. In particular, the texture contains two hyperbolic point defects and a $+1$ disclination ring. The dotted lines indicate the regions associated with the disclination ring. In panels b and d, the umbilic set consists of a fusiform tube connecting the point defects in the center and a closed loop corresponding to the disclination ring. The strength of the fusiform tube is $s = 2$, since each hue appears twice on a cross-section of the tube. For the loop, the strength is $s = 1$ and the longitudinal winding number is $k = 2$. The loop has a very small extent in the z direction, on the order of one or two lattice constants; therefore, determining its transverse index s is challenging at the given numerical resolution.

Consider a toron embedded in a uniform far field, and a planar section $\Sigma = \{y = y_0\}$ chosen such that it contains no singular points where the director is ill-defined. Since $\hat{\boldsymbol{n}}|_\Sigma$ approaches a constant (the far-field direction) at large in-plane distances, the section can be compactified by a point at infinity and defines a map $\Sigma \simeq S^2 \to S^2$ (after a continuous choice of the $\hat{\boldsymbol{n}} \sim -\hat{\boldsymbol{n}}$ lifting on the section, when needed). The skyrmion number

$$Q = \frac{1}{4\pi} \int_\Sigma \hat{\boldsymbol{n}} \cdot \left(\partial_x \hat{\boldsymbol{n}} \times \partial_z \hat{\boldsymbol{n}}\right) dx\, dz \tag{40}$$

is therefore well defined and integer-valued on such sections. Moreover, Q cannot change under a continuous translation of the section parameter y_0 unless the section crosses a genuine singularity (e.g., a point defect core) or the far-field boundary condition changes. Hence Q is constant for all admissible sections and, in particular, equals the value on a plane placed far from the soliton, where the director is uniform; therefore $Q = 0$ for any section Σ not intersecting singular cores.

The same conclusion follows from the Machon–Alexander relation between skyrmion number and umbilic intersections. For a compactified section Σ on which the spin-2 field is well defined away from umbilics, the weighted intersection sum satisfies (37). In the toron geometry the closed ring umbilic intersects Σ in two points with opposite intersection signs,

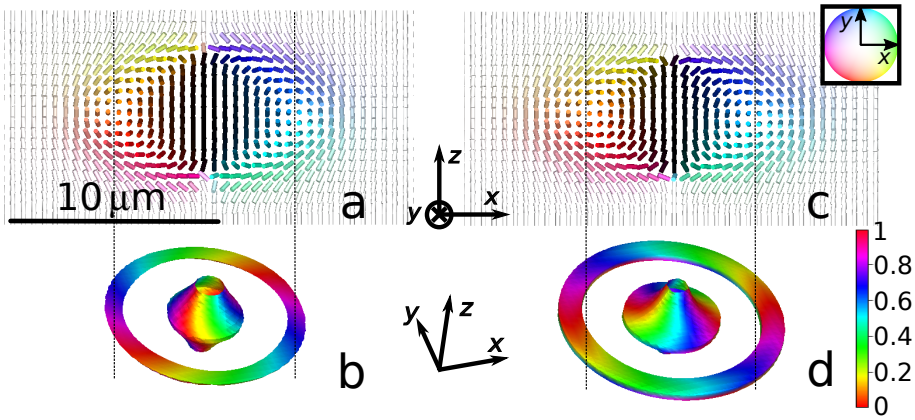

FIG. 1. Umbilic surfaces in torons. Director fields (a and c) and isosurfaces for ε (b and d) for the toron structure: a and c – director field distributions in the xz plane (the middle cross-section of the cell at $y = 0$). The color palette in the inset describes the x and y projections of the director used in a and c. This color wheel represents the northern hemisphere of director orientations where n_z is non-negative. In the southern hemisphere, the colors become darker as n_z decreases approaching the southern pole with $n_z = -1$. a – the structure obtained by the energy minimization, c – ansatz for toron. b – umbilic surfaces (isosurfaces for ε), $\varepsilon = -2.64$, d – umbilic surfaces for ansatz, $\varepsilon = -3.4$. The color bar shows the coloring method according to Eq. (34).

so its net contribution to the sum vanishes. In addition, there exists an umbilic line that closes through the far field (equivalently, through the compactification point at infinity); for any generic section Σ it also intersects the plane in two points with opposite signs, and therefore contributes zero net intersection number. Consequently, the total weighted intersection sum vanishes and the Machon–Alexander formula again yields $Q = 0$, consistent with the homotopy argument above.

Fig. 2 shows the results for the simulated CF1-loop structure obtained from the lattice model. This texture contains only smooth director deformations. The simulated CF1-loop configuration is characterized by continuous isolines forming closed loops. These isolines are not linked, indicating a trivial Hopf index $Q_H = 0$. The skyrmion number is also zero, $Q = 0$.

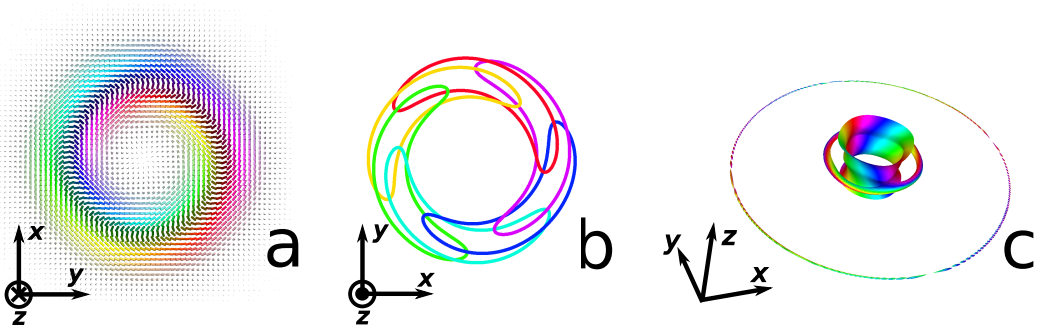

FIG. 2. Umbilic surfaces in the CF1-loop structure. a – director distribution in the xy plane (the middle cross-section of the cell at $z = 0$). b – isolines for the z projection of the director in the xy plane. c – umbilic surfaces for $\varepsilon = -4.2$. The color wheel and the color bar are the same as in Fig. 1.

The umbilic set consists of a broad central tube and two additional loops. The presence of the central tube indicates that the director field in the core region of CF1-loop is nearly homogeneous. In contrast to the toron, the tube here is wide, suggesting an extended region of quasi-uniform director field. The strength of the tube is $s = 2$, since each hue appears twice on a cross-section of the tube. Each of the two loops has strength $s = 1$ and longitudinal winding number $k = 2$. For the CF1-loop structure, there is no point defects. If we again pull the boundary to a point, the central tube transforms to a closed loop without any defects. It means that for the cross-section by the plane $\Sigma = \{z = z_0\}$ the closed loop formed by the central tube intersects the plane Σ twice. In each intersection the strength $s = 2$, but due to the orientation of this umbilic surface the transverse indices $\mathrm{index}_{D_p} U$ in intersections have opposite signs. So the closed to infinity central tube gives zero input to the left hand side of Eq. (37). It means that $Q = 0$ for this cross-section of the CF1-loop. Note, that we should not consider here the cross section Σ with $z = 0$ as in this plane the Machon–Alexander formula (37) is not applicable.

This example highlights the importance of accounting for "infinitely remote" umbilics (or, in a finite simulation box, umbilic sets supported near the domain boundary) when using umbilic-intersection formulas to compute the skyrmion index. If one were to keep only the "central" tubular component while ignoring the boundary-supported continuation required by the uniform far field, the weighted intersection sum would generally produce a spurious nonzero value for Q, in contradiction with the homotopy argument and with the direct evaluation of Eq. (37). In a finite computational domain, the "umbilic at infinity" is represented by an extended, smeared umbilic surface (or tube) distributed along the boundary region where the spin-2 field becomes ill-conditioned, and its intersections are essential for the cancellation of the total signed intersection number.

Fig. 3 illustrates how the umbilic set evolves as the isovalue is varied. At low ε the umbilic structure appears as two thin tubes, while at higher ε it becomes two loops. The petal-like features at the edges of panel e are artifacts caused by the finite sample boundary and can be ignored. In panel f, each loop has longitudinal winding number $k = 2$ and the strength $s = 1$. As ε is increased further, the isosurfaces begin to merge and the associated topological features can no longer be cleanly assigned to individual components. This behavior is typical in practical visualization: sufficiently small ε isolates individual umbilic cores, while larger ε probes a coarser, more "global" organization of the texture.

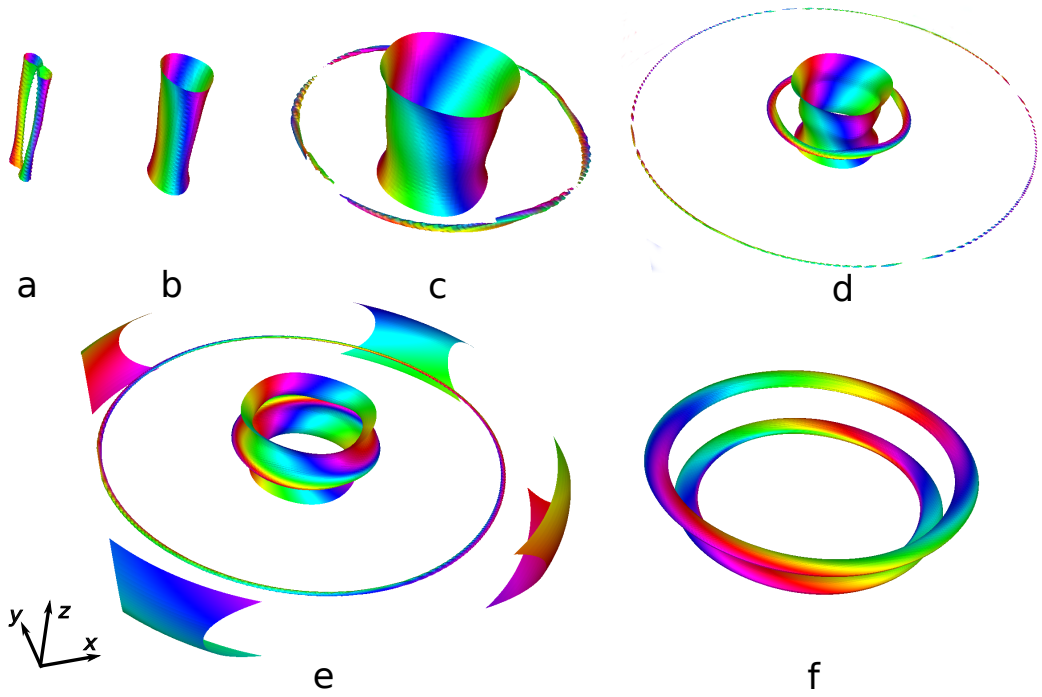

FIG. 3. Umbilic surfaces in the CF1-loop structure. Isosurfaces for different values of ε: a, b, c, d, e, f are umbilic surfaces at $\varepsilon = -7.5$, $\varepsilon = -6.5$, $\varepsilon = -4.85$, $\varepsilon = -4.2$, $\varepsilon = -3.6$, $\varepsilon = -0.65$. The scale in panels a, b and c is doubled. The color bar is the same as in Fig. 1.

Using Fig. 4 we analyze the topological features of the CF2-loop obtained by energy minimization. The relaxed configuration is characterized by looped and linked isolines (Fig. 4b, c). Depending on the director-field structure, the isolines can be linked with different handedness; in our case $Q_H = 1$. The hopfion also contains two disclination lines.

The umbilic set resembles that of CF1-loop: we again observe a wide central tube and two loops. The central tube for the CF2-loop is similar to one for the CF1-loop. However, the associated indices for two loops are different from the same loops in the CF1-loop. On Fig. 4d–f one can see that the hues progress of the inner and outer umbilic loops are different. It means that both umbilic loops for any plane Σ has the strength $s = 1$, but due to different orientation the transverse indices $\mathrm{index}_{D_p} U$ in intersections have opposite signs. Different orientation of the inner and outer umbilic loops gives the different direction of traversal in Eq. (39) when calculating the indices k. It gives $k = 2$ for the inner umbilic loop and $k = -2$ for the outer umbilic loop.

In the case of CF2-loop, we can see that two topological indices are related because the orientation of the umbilic line introduced for transverse index determines the direction of traversal for longitudinal winding. If one aims to resolve or compare different topological structures, the umbilic-surface representation provides additional discriminating information, since it exposes not only the presence of closed umbilic loops but also their transverse indices and longitudinal windings.

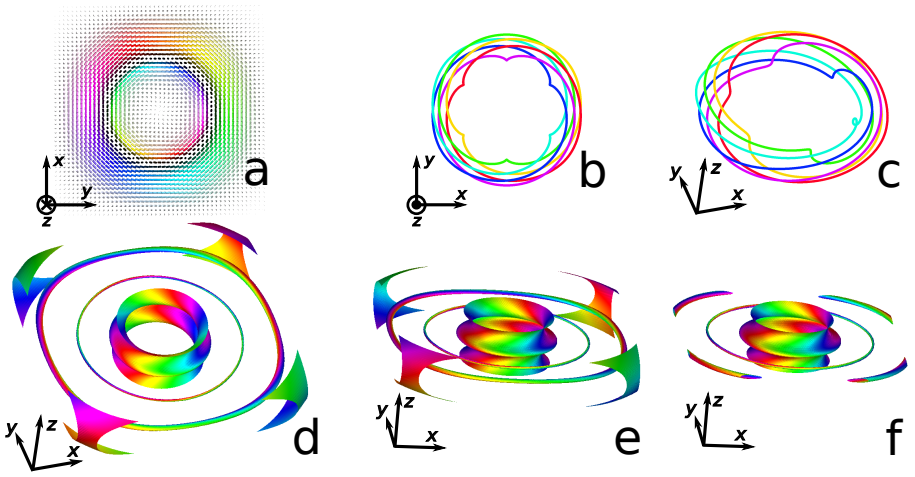

FIG. 4. Umbilic surfaces in the CF2-loop. a – director distribution in the xy plane (the middle cross-section of the cell at $z = 0$). b and c – isolines for the z projection of the director in the xy plane and from another viewpoint. d, e, and f – umbilic-surface representation with $\varepsilon = -3.4$. Panel f shows a cross-section of the isosurfaces from panel e. The color wheel and the color bar are the same as in Fig. 1.

7. Discussion

The overall motivation for using umbilics is that they offer a compressed representation of a three-dimensional director field. The proposed characterization of umbilics in terms of longitudinal and transverse charges makes it possible to avoid a detailed inspection of the full three-dimensional director field while still extracting topological information about the texture and its cross-sections. In particular, the transverse winding of the phase captures the local strength of each umbilic line, while the longitudinal winding along a closed umbilic loop captures a distinct invariant linked to the three-dimensional soliton topology. Taken together, these two integers provide a compact descriptor that connects directly to familiar global charges such as the skyrmion number.

The practical limitation in analyzing topological features is set by lattice resolution. The proposed color scheme is defined on the discrete grid: effectively, only one hue is assigned per lattice spacing. If the number of lattice points is insufficient—for instance, near highly localized structures or near singular regions—reliable extraction of the winding becomes difficult. In such cases the resolution must be increased. This is straightforward when working with analytical ansatzes, whereas in full numerical minimization increasing the number of nodes inevitably makes the search for equilibrium configurations more computationally expensive. In practice, this motivates using umbilic surfaces both as a visualization tool and as a diagnostic of whether the chosen discretization is adequate for robust topological readout.

We have considered, following Machon and Alexander [19], umbilic lines and their topological indices using the director field. However, a more accurate description of topological structures can be obtained by considering the tensor order parameter. It is of interest to generalize the Machon and Alexander umbilic lines analysis starting from the tensor order parameter.

Note that umbilics and disclination lines represent different types of line objects. A disclination line is associated with a breakdown of orientational order, typically via a singularity or a vanishing order parameter. In contrast, an umbilic is a region in which the transverse gradients of the director are isotropic: it is defined by a degeneracy of the transverse "principal curvatures" rather than by a loss of order. In some cases these objects can coincide. For example, for a λ disclination line (e.g., $\lambda^{1/2}$), sufficiently close to the line the orientational structure becomes independent of direction and depends only on the distance to the line, which is precisely the umbilic condition. This coincidence of λ-type disclination lines with umbilics follows from the symmetry structure of the elastic energy (1). Conversely, the presence of an umbilic does not imply a defect or a loss of order. In the degenerate case of a completely homogeneous director configuration, the entire region is umbilic, yet no disclination lines are present. In this sense, an umbilic can be viewed as a generalized disclination concept that also admits a zero charge.

Accurate localization of umbilics is challenging because it amounts to finding the zeros of a scalar field with high precision. Instead, one can vary the parameter ε in Eq. (14) and construct isosurfaces for successive values of ε, effectively foliating the domain by a family of level sets. The topological charges can then be evaluated on each surface. If a surface encloses an umbilic line, it must carry the same charges as that line. For sufficiently large ε, distinct isosurfaces begin to merge; the charges of the merged components combine accordingly, both longitudinally and transversely. Analyzing the charges of isosurfaces at larger ε may therefore provide additional information about soliton structure and can simplify the computation of topological charges for specific textures. More broadly, viewing umbilics through the evolution of

ε-level sets provides a convenient multiscale perspective: small ε isolates individual umbilic cores, while larger ε probes how these cores assemble into the global geometry of a three-dimensional soliton.

8. Conclusion

In this paper, we have developed the numerically robust modification of the umbilic-lines approach that provides a useful framework for analyzing three-dimensional topological structures in liquid crystals, magnets, and other anisotropic media supporting topological solitons. Our method yields a stable numerical realization of the Machon-Alexander umbilic invariant that is tailored to high-resolution three-dimensional simulations. It is based on the projector-symmetrization construction that defines the umbilic scalar field (13) whose near-vanishing identifies umbilic cores. The associated complex structure (18) is found to produce a natural phase field whose windings recover the two fundamental integer charges. The modified method requires only first derivatives, involves no gauge choice, and is, therefore, ideally suited for high-resolution three-dimensional computations of umbilic geometry in realistic simulated textures. We have demonstrated the efficiency of the method by using it to visualize the three topologically nontrivial structures: the toron, the cholesteric finger loop of the first type, and the cholesteric finger loop of the second type.

References

[1] Kleman M., Lavrentovich O.D. *Soft matter physics: an introduction*. Springer, New York, 2003.

[2] Chen B.G.G., Ackerman P.J., Alexander G.P., Kamien R.D., Smalyukh I.I. Generating the Hopf fibration experimentally in nematic liquid crystals. *Phys. Rev. Lett.*, 2013, **110**, P. 237801.

[3] Ackerman P.J., Smalyukh I.I. Diversity of knot solitons in liquid crystals manifested by linking of preimages in torons and hopfions. *Phys. Rev. X*, 2017, **7**, P. 011006.

[4] Oswald P., Baudry J., Pirkl S. Static and properties of cholesteric fingers in electric field. *Physics Reports*, 2000, **337**, P. 67.

[5] Ackerman P.J., Trivedi R. P., Senyuk B., van de Lagemaat J., Smalyukh I.I. Two-dimensional skyrmions and other soliton structures in confinement-frustrated chiral nematics. *Phys. Rev. E*, 2014, **90**, P. 012505.

[6] Afghah S., Selinger J.V. Theory of helicoids and skyrmions in confined cholesteric liquid crystals. *Phys. Rev. E*, 2017, **96**, P. 012708.

[7] Durey G., Sohn H.R.O., Ackerman P.J., Brasselet E., Smalyukh I.I., Lopez-Leon T. Topological solitons, cholesteric fingers and singular defect lines in Janus liquid crystal shells. *Soft Matter*, 2020, **16**(11), P. 2669–2682.

[8] Smalyukh I.I. Knots and other new topological effects in liquid crystals and colloids, *Rep. Prog. Phys.*, 2020, **83**, P. 106601.

[9] Wu J.-S., Smalyukh I.I. Hopfions, heliknotons, skyrmions, torons and both abelian and nonabelian vortices in chiral liquid crystals. *Liquid Crystals Reviews*, 2022, **10**(1-2), P. 34.

[10] Tambovtsev I.M., Leonov A.O., Lobanov I.S., Kiselev A.D., Uzdin V.M. Topological structures in chiral media: effects of confined geometry. *Phys. Rev. E*, 2022, **105**, P. 034701.

[11] Hamdi R., Petriashvili G., Lombardo G., De Santo M.P., Barberi R. Liquid crystal bubbles forming a tunable micro-lenses array. *J. Appl. Phys.*, 2011, **110**, P. 074902.

[12] Yang B., Brasselet E. Arbitrary vortex arrays realized from optical winding of frustrated chiral liquid crystals. *J. Opt.*, 2013, **15**, P. 044021.

[13] Hess A.J., Poy G., Tai J.S.B., Žumer S., Smalyukh I.I. Control of light by topological solitons in soft chiral birefringent media. *Phys. Rev. X*, 2020, **10**, P. 031042.

[14] Ackerman P.J., Qi Z., Smalyukh I.I. Optical generation of crystalline, quasicrystalline, and arbitrary arrays of torons in confined cholesteric liquid crystals for patterning of optical vortices in laser beams. *Phys. Rev. E*, 2012, **86**, P. 021703.

[15] Nagaosa N., Tokura Y., Topological properties and dynamics of magnetic skyrmions. *Nat. Nanotechnol.*, 2013, **8**, P. 899–911.

[16] Lobanov I.S., Uzdin V.M. Lifetime, collapse, and escape paths for hopfions in bulk magnets with competing exchange interactions. *Phys. Rev. B*, 2023, **107**, P. 104405.

[17] Chichay K.A., Lobanov I.S., Uzdin V.M. The structure of magnetic domain walls in cylindrical nano- and microwires with inhomogeneous anisotropy. *Nanosystems: Phys. Chem. Math.*, 2024, **15**(1), P. 55–59.

[18] Chichay K.A., Lobanov I.S., Uzdin V.M. Magnetic structure of domain walls in stressed cylindrical wires. *Nanosystems: Phys. Chem. Math.*., 2025, **16**(3), P. 325–332.

[19] Machon T., Alexander G.P. Umbilic lines in orientational order. *Phys. Rev. X*, 2016, **6**(1), P. 011033.

[20] Selinger J.V. Interpretation of saddle-splay and the Oseen-Frank free energy in liquid crystals. *Liquid Crystals Reviews*, 2018, **6**(2), P. 129.

[21] Tai J.-S.B., Ackerman P.J., Smalyukh I.I. Topological transformations of Hopf solitons in chiral ferromagnets and liquid crystals. *Proc. Natl. Acad. Sci.*, 2018, **115**(5), P. 921–926.

[22] Tai J.-S.B., Wu J.-S., Smalyukh I.I. Geometric transformation and three-dimensional hopping of Hopf solitons. *Nat. Commun.*, 2022, **13**(1), P. 2986.

[23] Foster D., Kind C., Ackerman P.J., Tai J.-S.B., Dennis M.R., Smalyukh I.I. Two-dimensional skyrmion bags in liquid crystals and ferromagnets. *Nat. Phys.*, 2019, **15** (7), P. 655–659.

[24] Varanytsia A., Posnjak G., Mur U., Joshi V., Darrah K., Muševič I., Čopar S., Chien L.-C. Topology-commanded optical properties of bistable electric-field-induced torons in cholesteric bubble domains. *Sci. Rep.*, 2017, **7**(1), P. 16149.

[25] Pirkl S., Ribière P., Oswald P. Forming process and stability of bubble domains in dielectrically positive cholesteric liquid crystals. *Liq. Cryst.*, 1993, **13** (3), P. 413–425.

[26] Trivedi R.P., Lee T., Bertness K.A., Smalyukh I.I. Three dimensional optical manipulation and structural imaging of soft materials by use of laser tweezers and multimodal nonlinear microscopy. *Opt. Express*, 2010, **18**, P. 27658–27669.

[27] Shen Y., Dierking I. Electrically driven formation and dynamics of skyrmionic solitons in chiral nematics. *Phys. Rev. Appl.*, 2021, **15**, P. 054023.

[28] de Gennes P.G., Prost J. *The Physics of Liquid Crystals*. Clarendon Press, Oxford, 1993.

[29] Ravnik M., Žumer S. Landau-de Gennes modelling of nematic liquid crystal colloids. *Liq. Cryst.*, 2009, **36**, P. 1201–1214.

[30] LCSim, 2021–2026, https://gitlab.com/alepoydes/lcsim.

[31] Pollard J., Posnjak G., Čopar S., Muševič I. and Alexander G.P. Point defects, topological chirality, and singularity theory in cholesteric liquid-crystal droplets. *Phys. Rev. X*, 2019, **9**, P. 021004.

[32] Lobanov I., Aksenova E., Orlova T., Darmoroz D., Uzdin V., Kiselev A.D. Optical imaging and analytical design of localized topological structures in chiral liquid crystals. *Symmetry*, 2022, **14**(12), P. 2476.
[33] Shvetsov S.A., Darmoroz D.D., Vasil'ev A., Orlova T., Lobanov I.S., Rafayelyan M. Light-induced isotropic pen for generation of topological solitons and hopfion–toron transition in frustrated chiral nematic films. *Chaos, Solitons & Fractals*, 2025, **199**(3), P. 116905.
[34] Strömer J.F., Raynes E.P. Study of elastic constant ratios in nematic liquid crystals. *Appl. Phys. Lett.*, 2006, **88**, P. 051915.
[35] Bennett T., Proctor M., Kaczmarek M., D'Alessandro G. Lifting degeneracy in nematic liquid crystal viscosities with a single optical measurement. *J. Colloid Interface Sci.*, 2017, **497**, P. 201–206.

Submitted 16 December 2025; revised 20 January 2026; accepted 23 January 2026

Information about the authors:

Elena V. Aksenova – Saint Petersburg State University, 199034, 7-9 Universitetskaya Emb., Saint Petersburg, Russia; ORCID 0000-0002-4324-1491; e.aksenova@spbu.ru

Igor S. Lobanov – ITMO University, 197101, Kronverksky Pr. 49, Saint Petersburg, Russia; ORCID 0000-0001-8789-3267; lobanov@itmo.ru

Tetiana Orlova – Yerevan State University, 1 Alex Manoogian, Yerevan, 0025, Armenia; ORCID 0000-0002-1594-291X; tetiana.orlova@ysu.am

Valery M. Uzdin – ITMO University, 197101, Kronverksky Pr. 49, Saint Petersburg, Russia; ORCID 0000-0002-9505-0996; vmuzdin@itmo.ru

Alexei D. Kiselev – ITMO University, 197101, Kronverksky Pr. 49, Saint Petersburg, Russia; ORCID 0000-0002-1023-3284; adkiselev@itmo.ru

Conflict of interest: the authors declare no conflict of interest.